CALIBRATION OF THE FORWARD MUON DETECTOR AT H1

V.L.Hudgson

High-Energy Physics Group,
School of Physics and Space Research,
Faculty of Science,
The University of Birmingham.

Mid-term Report

January 1995

Abstract

The H1 detector started taking data at the HERA collider in 1992. HERA collides 27.5 GeV electrons with 820 GeV protons, and thus extends previously accessible kinematic regions by two orders of magnitude. Due to the asymmetric beam energies H1 has enhanced instrumentation in the forward (proton) direction, which includes the forward muon detector (FMD), designed to detect muons boosted in the forward direction.

This report contains an overview of the physics potential of HERA, followed by a general description of the H1 detector. The work carried out to align the drift chambers of the forward muon system is described, together with the results of alignment, and checks carried out on the alignment procedure. Studies involving two calibration parameters of the FMS, drift velocity and T-zero, are discussed. Finally, a preliminary investigation into the dimuon decay of elastic J/ψ's is included.

Contents

List of Figures

List of Tables

Chapter 1

Introduction

1.1 The Standard Model

The fundamental structure of matter is described in terms of a theory known as the Standard Model. In this theory the fundamental building blocks of matter are the spin $\frac{1}{2}$ fermions, and the interactions between these particles are mediated by spin 1 gauge bosons. The four fundamental forces of nature are known as the strong, weak, electromagnetic and gravitational forces, but the last of these, the gravitational force, is not included in the Standard Model. This is due to problems arising in its formulation as a quantum field theory, but at the energies of interest to particle physics the strength of the gravitational force is so small that its inclusion in the Standard Model can be safely neglected.

The fermions are divided into two classes, known as quarks and leptons, the difference between them being that the quarks experience the strong force, whereas the leptons do not. These quarks and leptons are grouped into three families or generations, shown in table 1.1. There are six flavours of quark, three with a charge of +2/3 (u, c, t) and three with a charge of -1/3 (d, s, b). Each lepton family consists of a negatively charged particle (e, μ, τ) and its corresponding massless and uncharged neutrino $(\nu_e, \nu_\mu, \nu_\tau)$.

	Generations		
Quarks	u	c	t
	d	s	b
Leptons	e	μ	τ
	ν_e	ν_μ	ν_{tau}

Table 1.1: *The three generations of fermions*

Members of the lightest of these three generations of fermions (e, u, d) make up the stable matter observed in nature. In the other generations there are more massive particles which are unstable and eventually decay via the weak interaction. It has been shown experimentally that only three generations exist, although it is not understood why.

The fundamental forces of nature are described in the Standard Model by Gauge Field Theories, where the interactions are interpreted as the exchange of virtual bosons. The fermions are represented by complex fields in quantum field theory, and these fields are used to construct an expression describing the energy - momentum dynamics of the system, called the Lagrangian. It is postulated that the Lagrangian remains invariant under a local gauge transformation. However, extra terms are introduced to the quantum field theory Lagrangian when it undergoes a local gauge transformation, and to restore the invariance it is necessary to add a new field to the original Lagrangian. It is this field which describes the gauge boson.

The first interaction to be explained in this way was the electromagnetic interaction, described by the quantum field theory known as Quantum Electrodynamics (QED) and is mediated by a massless gauge boson called the photon. Since the photon is massless the electromagnetic force has an infinite range. The success of this theory led to the application of gauge theories to describe other fundamental forces.

Weak interactions are mediated by the exchange of massive gauge bosons W^+, W^- and Z^0, and was first postulated to explain certain phenomena, such as beta decay. This force was unified with the electromagnetic interaction by the Glashow-Weinberg-Salam (GWS) electroweak theory in the late 1960's. This model combines these interactions in one framework, although at observable energies they have very different strengths.

Finally, the strong interaction is described by a quantum field theory known as Quantum Chromodynamics (QCD). This interaction is mediated by an octet of massless and chargeless gluons, and is responsible for binding quarks into hadrons. The gluons, like the quarks, carry a 'colour charge', and so may interact with each other. The quarks are never observed in isolation, but always confined in hadrons. This is an observed property of QCD, known as colour confinement, where only particles which are colour singlets may be observed directly.

1.2 The HERA Accelerator

The HERA (**H**adron **E**lectron **R**ing **A**nlage) collider at DESY is the first electron (positron) - proton collider to be built. It consists of two independent accelerators, designed to accelerate and store 820 GeV protons and 30 GeV electrons, and collide the counter rotating beams at four interaction points arranged symmetrically around the 6.3 km circumference. At these interaction points the bunch crossing interval is 96 ns, to produce the design luminosity of 1.5×10^{31} cm^{-2} s^{-1}. At design luminosity there will be 210 electron and proton bunches colliding with total beam currents of 60 and 160 mA respectively. Whilst the superconducting proton ring has reached its design energy, the electron ring is presently operating at 27.5 GeV.

The nominal electron and proton beam energies give a centre of mass energy of approximately 310 GeV, an improvement by an order of magnitude on previous fixed target experiments, and this gives HERA enormous physics potential. The current HERA parameters are shown in figure 1.1.

Lumi System

HERA and H1 Operation

Parameter	Units	1992	1993	1994		
				e^-p	e^+p	sh.IP
$\mathcal{L}$ (HERA produced)	[nb^{-1}]	?	999	938	4977	86
$\mathcal{L}$ (HERA physics)	[nb^{-1}]	55	880	846	4665	78
$\mathcal{L}$ (H1 taken)	[nb^{-1}]	30	568	532	3509	67
$\mathcal{L}$ (H1 physics)	[nb^{-1}]	25	528	494	3424	65
HERA efficiency	[%]	?	88	90	94	91
H1 efficiency	[%]	46	60	58	73	83
Average lumi	[10^{30} cm^{-2}s^{-1}]	0.028	0.27	0.62	1.29	0.98
Max peak lumi	[10^{30} cm^{-2}s^{-1}]	0.22	1.3	2.6	4.3	2.1
$< I(p) >$	[mA]	0.94	10.8	28.6	41.0	41.2
$< I(e) >$	[mA]	1.33	7.7	10.5	17.0	16.8
Number of colliding bunches		9	84	153	153	153
Number of pilot (e,p) bunches		1,1	10,6	15,17	15,17	15,17
Number of HERA Lumi runs		132	218	116	169	7
Number of permanent H1 runs		1409	3190	1141	1816	40
First H1 run		24601	50673	76345	82961	89929
Last H1 run		36008	66609	82005	90419	90026
Average H1 run duration	[sec]	973	817	1115	1620	1721

Summary

Figure 1.1: *Parameters of H1 and the HERA accelerator*

1.3 HERA Physics

The high centre of mass energies available at HERA mean that previously accessible kinematic regions are extended by two orders of magnitude. With four momentum transfers squared (q^2) of the order of 10^4, deep inelastic scattering events down to x values of 10^{-4} are directly measurable, extending our knowledge of the internal structure of the proton. This creates an ideal testing ground for aspects of the standard model, particularly QCD. Other areas of physics potential include photoproduction, heavy flavour physics, electroweak physics and searches for exotic particles [1][2]. These will all be discussed in greater detail in the following sections.

1.3.1 Deep Inelastic Scattering (DIS)

The deep inelastic scattering process $ep \longrightarrow e(\nu)X$ can be considered in two stages. Firstly, there is quasi-elastic scattering of the the electron by one of the proton's constituents, partons, carrying a fraction, x, of the proton's 4-momentum. DIS cross-sections are governed by proton structure functions which describe the density distributions of charged partons of fractional momentum x. Secondly, hadronization of the struck parton and proton remnant partons occurs in which the final products are the colour singlet hadrons. The kinematics of this process are shown in figure 1.2.

The process can be described by two variables, conventionally chosen from Q^2 and the scaling quantities x and y, only two of which are independent. The quantity Q^2 is the square of the four-momentum transfer between the incoming and outgoing leptons. In the naive quark parton model (QPM), x is the fraction of the proton momentum carried by the struck parton (Bjorken x), and y is the fraction of energy transfered to the hadronic system from the incoming electron. In Lorentz invariant notation, these variables are given by:

$$Q^2 = -q^2 = -(k - k^{'})^2 \tag{1.1}$$

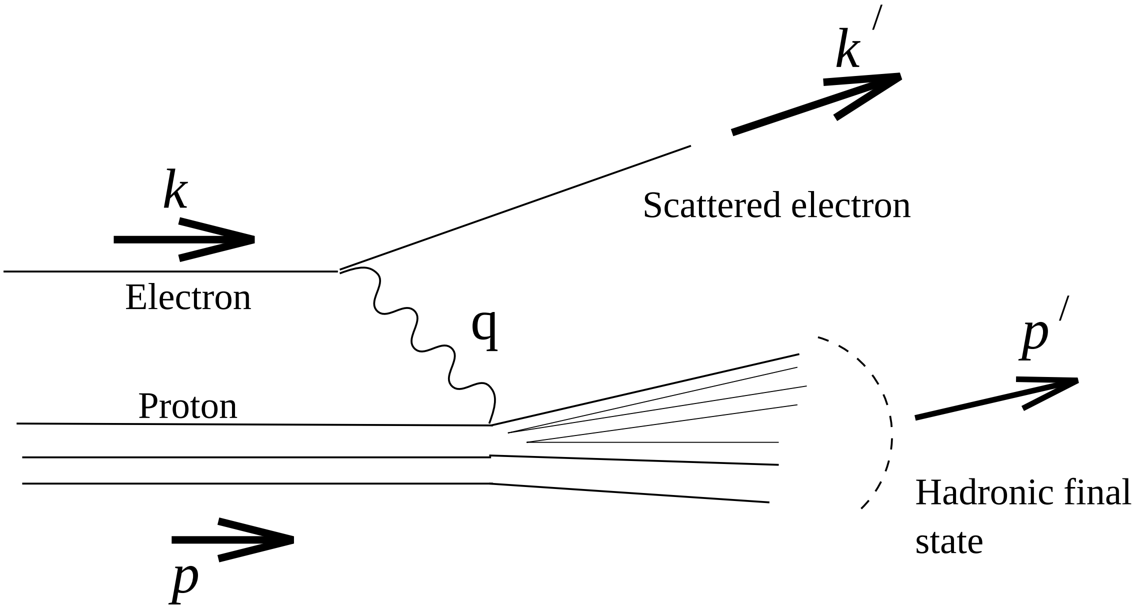

Figure 1.2: *Diagram showing the kinematics of electron - proton scattering.*

$$x = \frac{Q^2}{2P \cdot q} \tag{1.2}$$

$$y = \frac{P \cdot q}{P \cdot k} \tag{1.3}$$

where k, $k^{'}$ and P are the four-momentum vectors of the incoming lepton, outgoing lepton, and the incoming proton respectively, and q is the four-momentum vector of the virtual exchange particle. These quantities are related by the equation:

$$Q^2 = xys \tag{1.4}$$

where s is the centre of mass energy squared, and is defined as:

$$s = (k + P)^2 \simeq 4EE_P \tag{1.5}$$

E and E_P are the energies of the incoming electron and proton respectively. Neglecting the proton mass, the invariant mass squared, W^2, of the hadronic final state is:

$$W^2 = (q + P)^2 = Q^2 \frac{1 - x}{x} \tag{1.6}$$

This is a useful quantity to define for charged current events, where the outgoing neutrino is not observed, making it necessary to look at the kinematics of the hadronic final state instead.

The kinematic variables measured to describe charged lepton - nucleon scattering are the polar angle, θ, and the energy, $E^{'}$, of the scattered lepton. The variables x, y and Q^2 in terms of these variables are:

$$Q^2 = 4EE^{'} cos^2 \left(\frac{\theta}{2}\right) \tag{1.7}$$

$$y = 1 - \frac{E^{'}}{E} sin^2 \left(\frac{\theta}{2}\right) \tag{1.8}$$

$$x = \frac{Q^2}{sy} \tag{1.9}$$

The unique kinematic range accessible at HERA allow the structure functions of the proton to be measured down to very small values of x ($x \sim 10^{-4}$). The behaviour of the structure function, F_2 is well described by the perturbative QCD evolution equations of Gribov, Lipatov, Altarelli and Parisi (GLAP). However, at low x ($10^{-4} < x < 10^{-1}$), this is less successful, and F_2 is better described by the Balitskii-Kuraev-Fadin- Lipatov (BFKL) equation which predicts a rise in F_2 with decreasing x, in agreement with recent observations at HERA. This rise is attributed to an increasing gluon density, and consequently a growing sea quark density, at low x [3].

1.3.2 Photoproduction

The low Q^2 region offers rich physics potential, allowing the structure of the photon to be probed in a new kinematic regime. Events involving the scattering of quasi-real photons with protons are classed as photoproduction events, and are characterized by $Q^2 \sim 0$, where the electron is scattered at low angles. These photoproduction events are the dominant process at HERA. The rate is large because the amplitude for $e \longrightarrow e\gamma$ diverges as $Q^2 \rightarrow 0$. At $W_{\gamma p} = 197$GeV (where $W_{\gamma p} \simeq 2\sqrt{E_\gamma E_p}$), the total photoproduction cross section measured was $156 \pm 2 \pm 18$ μb [4]. The total cross section for low Q^2 events contains contributions from direct and resolved hard scattering processes, and from soft processes, where the labels 'hard' and 'soft' refer to the transverse momenta, p_T, involved in the parton-parton process. Hard processes give rise to outgoing partons with p_T's of 1GeV or more, whilst soft processes have p_T's of a few hundred MeV or less.

Hard scattering processes where the photon couples point-like with a parton in the proton are known as 'direct' photon interactions. These interactions include QCD Compton scattering ($\gamma q \longrightarrow gq$) and photon gluon fusion ($\gamma q \longrightarrow q\bar{q}$), and are of interest since heavy flavour production occurs predominantly through photon gluon fusion as a result of the high cross section of low Q^2 events. Measurements of the cross section allow measurements to be made of the gluon density in the proton. Subprocesses where the photon couples to a $q\bar{q}$ pair (pair production) one of which in turn interacts with a gluon from the proton are known as resolved photoproduction processes, and are of interest as they probe the partonic nature of the photon, making possible measurements of the photon structure function. Hard scattering processes (direct or resolved) give rise to high transverse momentum jets and provide an ideal testing ground for perturbative QCD. Finally, in soft photoproduction processes, the photon fluctuates to a vector meson (ρ, ϕ, ω, ...) which then interacts with the proton.

1.3.3 Heavy Flavour Physics

Heavy flavour production at HERA is an important area, with an estimated 10^8 charmed hadrons and 10^6 B-hadrons produced per 100 pb^{-1} of integrated luminosity. Areas of interest include J/ψ and open charm production using easily identified decay modes of beauty and charm particles,

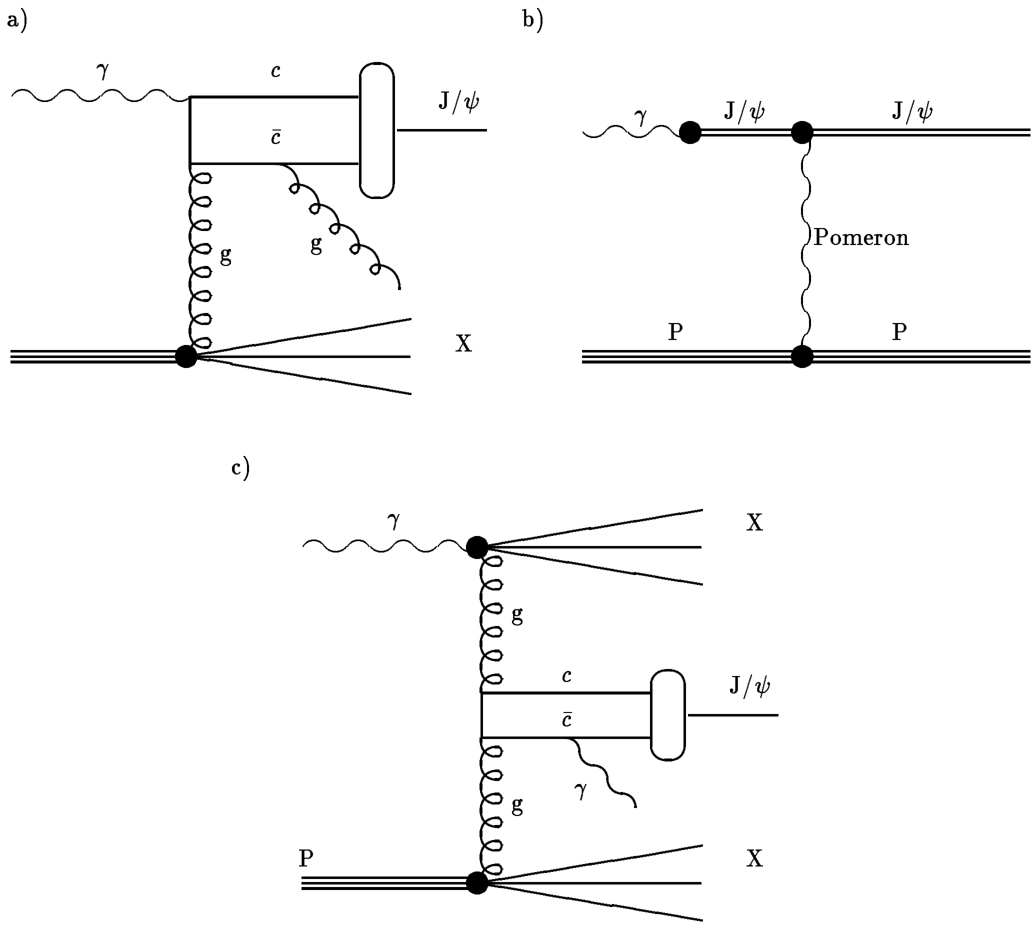

Figure 1.3: J/ψ production mechanisms

and in the longer term measurements of $\bar{B}^0 - B^0$ and $\bar{D}^0 - D^0$ mixing may be possible.

The main source of J/ψ production is through photon gluon fusion of the incoming photon with a gluon from the proton, which is well defined and calculable in perturbative QCD. The differential cross section for this process is given by:

$$\frac{d^2\sigma}{dx_{gluon}dt} = G(x_{gluon})\frac{d\sigma}{dt} \tag{1.10}$$

where t is the difference in four momentum between the initial photon and the final J/ψ meson, x_{gluon} is the fraction of the proton four momentum carried by the initial gluon, and $G(x_{gluon})$ is the gluon distribution function for the proton. Hence measurement of the cross section for inelastic J/ψ production can give information about the gluon density of the proton [5].

Other mechanisms include the photon coupling to a J/ψ which is then diffractively scattered by the proton. This soft diffractive process is considered to be due to the exchange of a pomeron, and allows the nature of pomeron and photon-hadron coupling to be studied. In the elastic diffractive case all that is observed in the detector is the lepton pair produced (if the J/ψ decays to two leptons; a process which has a branching ratio of approximately 12%). Also, the resolved photoproduction process may produce a $c\bar{c}$ pair which combine to form a J/ψ. These mechanisms are shown in figure 1.3. The total photoproducion cross section of J/ψ's was measured at HERA as [6]:

$$\sigma(\gamma p \longrightarrow J/\psi + X) = (56 \pm 13 \pm 14)nb$$

1.3.4 Electroweak Physics

Tests of electroweak physics are possible with full design luminosity at HERA, despite the extremely low cross section for the production of the electroweak bosons, $W^{\pm}$ and Z^0. It is estimated that a few tens of these particles should be produced for an integrated luminosity of 100 pb^{-1}; the measurements of the cross sections is an important test of the non-Abelian nature of the electroweak interaction.

1.3.5 Exotics

The HERA accelerator provides exciting new opportunities to search for new phenomena beyond the standard model. This includes searches for new particles, such as leptoquarks, excited leptons, supersymmetric particles and heavy Majorana neutrinos, and a search for new interactions through the appearance of small systematic deviations from the expected Standard Model cross sections. For masses up to 275GeV, there has been no significant evidence at H1 for the production of leptoquarks, leptogluons or squarks [7].

Chapter 2

The H1 Detector

2.1 General Overview

H1 [8] is one of the two general purpose detectors presently operating at HERA (see figure 2.1). It is built on the same principles as most modern collider experiments, differing in the enhanced instrumentation in the forward (proton) direction due to the asymmetric proton and electron beam energies. To maximize the full physics potential of HERA, the H1 detector has to satisfy certain basic requirements. A high degree of hermicity is important in order to investigate phenomena involving energetic neutrinos. Good electromagnetic and hadronic energy resolution is essential in the study of inclusive energy flow measurements and jet measurements for both neutral and charge current interactions. In order to study heavy flavour physics and to allow a search for new particles, good muon identification is also very important. The study of DIS process requires excellent electron identification and measurement. Adequate segmentation of the calorimeter in depth and in θ and ϕ is thus required. Finally, to make efficient use of all these facilities, a sophisticated trigger system is needed to overcome the very high background conditions experienced at H1.

The main components of the H1 detector are as follows:-

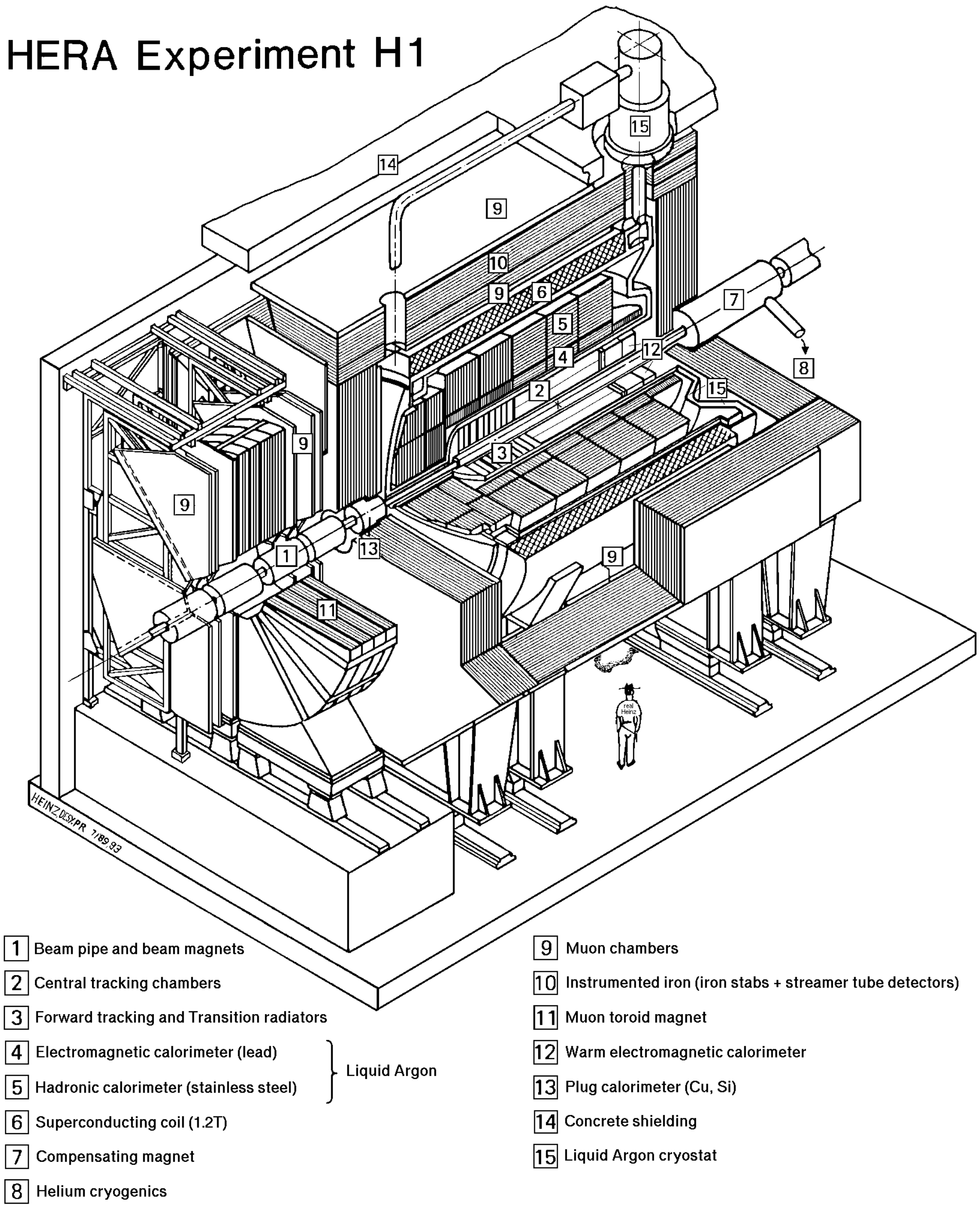

Figure 2.1: *The H1 Detector.*

- Tracking system divided into central and forward tracking detectors, which consist of several layers of drift chambers interspersed with multiwire proportional chambers for triggering, and additional backward drift chambers. Upgrades to H1 also include silicon tracking detectors close to the beam line in the central and backward regions.

- Calorimeter system includes a liquid argon calorimeter surrounding the tracker segmented into an electromagnetic part and a hadronic part, and a plug calorimeter to detect hadronic energy at very small angles in the forward direction. Spacal replaces the BEMC (backward electromagnetic calorimeter) and, together with the backward plug calorimeter, provides calorimetry for the backward region.

- A superconducting coil outside the hadronic calorimeter providing a magnetic field of 1.6 Tesla, enabling tracking of particles through the detector.

- Iron return yoke surrounding all the major components of H1, instrumented to allow measurement of hadronic energy and muon identification.

- Forward muon spectrometer consisting of layers of drift chambers either side of a toroidal magnet, providing identification and measurement of muons in the forward region.

- Electron and photon taggers used to measure luminosity. The electron tagger is also important for photoproduction events.

The rest of this chapter will discuss in greater detail the main features mentioned above, with particular emphasis on the forward muon detector with its relevance to this report.

2.2 Tracking

The tracking system at H1 has been designed to provide precise measurements of momentum and angle of isolated charged particles, and ability to reconstruct jets with high track densities. Many charged particles are produced at small angles in the forward direction due to the asymmetry in the energies of the electron and proton beams, and in order to facilitate good triggering and reconstruction over the whole solid angle, the tracking system is divided into two mechanically distinct tracking detectors: the central (CTD) and forward (FTD) trackers. Both detectors consist of drift chambers and multiwire proportional chambers. The drift chambers give accurate information on the trajectories of charged particles traveling through the magnetic field thus allowing a momentum measurement, and triggering information is provided by the proportional chambers in the central and forward regions. Particle identification is achieved by measuring the specific energy loss dE/dx, with a typical energy resolution of about 10%. The tracking system is shown in figure 2.2.

2.2.1 The Central Tracking Detector (CTD)

The CTD consists of two concentric drift chambers (CJC1 and CJC2) and covers the angular range $25^\circ < \theta < 155^\circ$. The sense wires are strung parallel to the beam direction, and drift cells inclined at 30° to the radial direction. This provides a good measurement of the position coordinate in the $r\phi$ plane, with a spatial resolution 170μm. Only a moderate z-position measurement can be achieved using charge division (approximately 1 % of the wire length).

Two thin 'z-chambers' (CIZ and COZ) sandwich the inner jet chamber and complement the measurement of charged track momenta made in the central chambers. These chambers have sense wires perpendicular to the beam axis, and provide a z-measurement with a resolution of typically 300μm. The polar angular range covered by the inner and outer z-chambers is $16^\circ <$

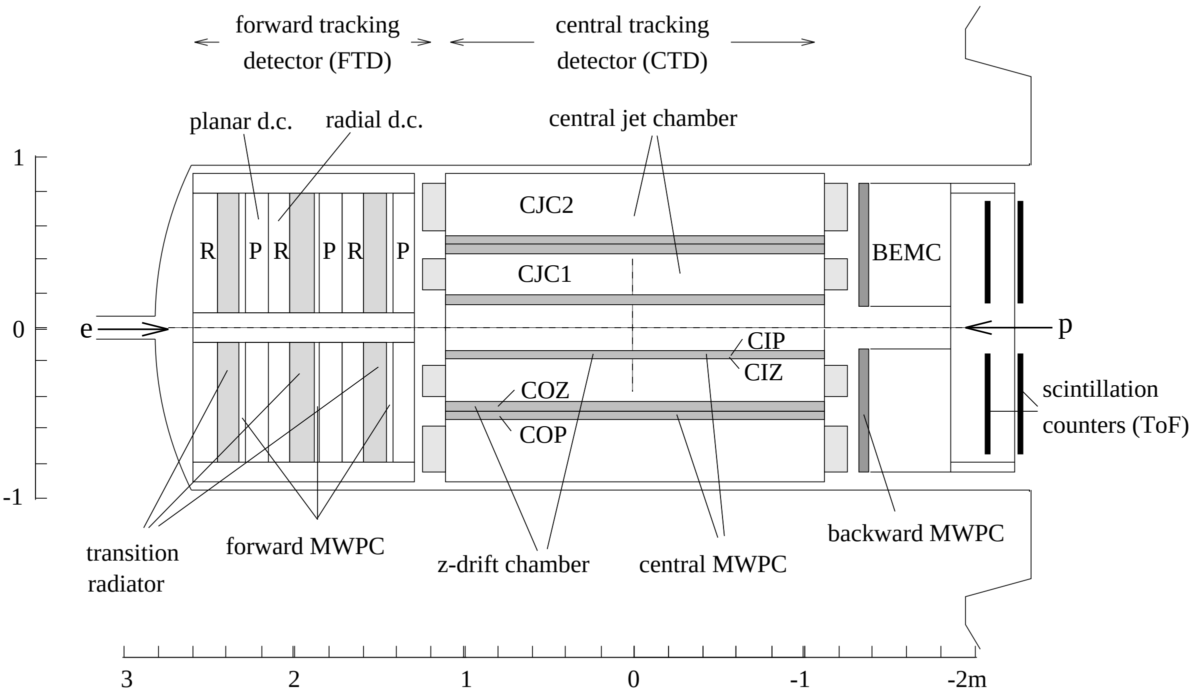

Figure 2.2: *The H1 tracking system ($r-z$ view).*

$\theta < 169°$ and $25° < \theta < 156°$ respectively.

Two multiwire proportional chambers, CIP and COP, are mounted inside the CIZ and outside the COZ respectively. These chambers consist of a double layer of anode wires, and their main purpose is triggering, providing a fast first level (L1) trigger decision which can be used to distinguish between successive beam crossings. The CIP and COP provide a polar angular coverage of $10° < \theta < 170°$ and $25° < \theta < 155°$ respectively.

2.2.2 The Forward Tracker (FTD)

The forward tracker was designed to provide an accurate measurement of charged particles in the forward direction, track information on individual particles, electron identification and a fast forward ray trigger. To achieve this, the detector consists of three supermodules covering an angular range $6^\circ < \theta < 25^\circ$. Each supermodule consists of planar drift chambers at orientations of 0°, 120° and 240° to give accurate space point reconstruction; a multiwire proportional chamber for triggering; a passive transition radiation detector used for electron identification; and a radial drift chamber to give an accurate $r\phi$ measurement. The resolutions of the FTD are 200μm in the $r\phi$ plane and 170μm in x and y coordinates.

2.2.3 Backward drift chambers

The backward drift chambers [9] are designed provide additional tracking in the backward region, measuring the impact point in front of the backward calorimeter to an accuracy of about 1mm. The detector consists of five octagonal layers, with half planes of drift chambers perpendicular to the beam axis. The five layers are rotated with respect to each other by an angle of 18°. The expected spatial resolutions are 0.4mm in r and 0.8mm in ϕ, with a double track resolution of 3mm. The expected resolution in the ionization loss measurement (dE/dx) is 30%.

2.2.4 Silicon Trackers

Heavy flavour physics, particularly the identification of heavy quark decays, requires the separation of primary and secondary vertices, which calls for a high resolution position sensitive detector very close to the interaction point. In order to explore the region of low x physics a measurement of the electron at small angles and at small energies is required. The introduction of the silicon detectors [10] should satisfy these requirements, with the central silicon tracker (CST) providing high resolution tracking and vertex reconstruction in the central region, and the backward silicon tracker (BST) measuring particles at small angles with respect to the electron beam.

The CST is situated in the innermost chamber of the central tracker, around the interaction point, and concentric with respect to the beam pipe. It consists of two barrel shaped layers of double sided silicon strip detectors, with an inner radius of 40mm and an outer radius of 75mm. The BST is situated behind the CST, in the backward portion of the central tracker, and consists of eight discs mounted perpendicular to the beam line. Each disc is comprised of three different layers: two strip detectors for tracking, and one with pad detectors for triggering. Both silicon tracking detectors should provide a spatial resolution of about 10μm.

2.3 Calorimetry

In a calorimeter, an incident particle induces a shower of particles in some 'absorber' material, and these particles can then be detected as they pass through some 'active' material. By measuring, for example, the amount of ionization in the active medium, the energy of the incident particle may be determined. A coil inside the calorimeter, would cause the the energy measurement of electromagnet showers to be degraded, and thus the requirements of clear identification of electrons, muons and penetrating neutral particles together with a need for a good performance in the measurement of jets with high particle densities, are best met by a calorimeter inside a large coil. This minimizes both the amount of dead material in front of the calorimeter, and the overall size.

2.3.1 Liquid Argon Calorimeter (LAC)

The choice of liquid argon for the calorimeter results from its stability, ease of calibration, the fine readout granularity that is possible, and the homogeneity of response. The LAC is segmented into an electromagnetic part and a hadronic part, and covers the angular range $4° < \theta < 153°$. The acceptance of the electromagnetic part is slightly greater in the backward region than the hadronic part. The entire system is divided in z into eight self supporting

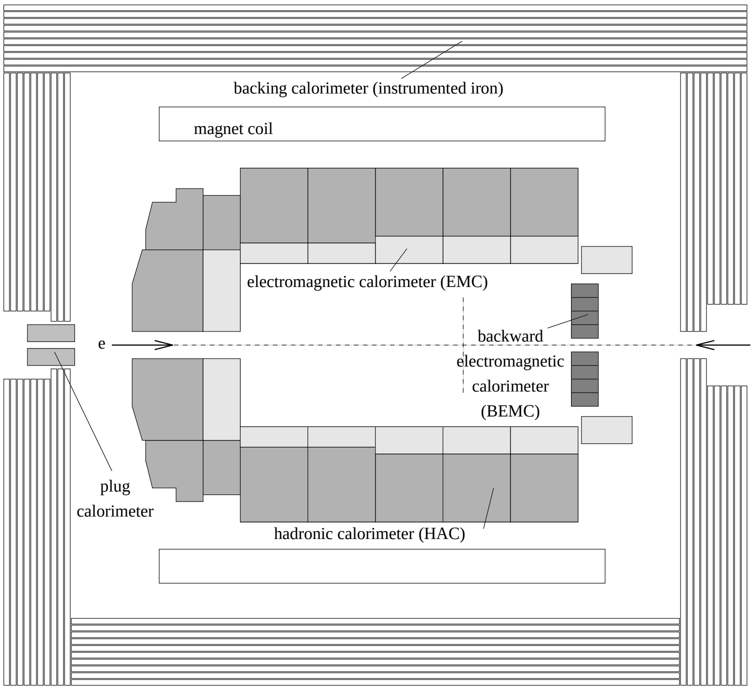

Figure 2.3: *The Calorimetry system of the H1 Detector.*

'wheels', with each of the six barrel wheels divided in ϕ into eight identical octants, called stacks. Each stack is in turn segmented into electromagnetic and hadronic parts, which use lead absorption and stainless steel absorption plates respectively, with gaps filled with liquid argon as the active medium. The energy resolution, σ(E)/E is between 10% and 13%/$\sqrt{E}$, with a constant term below 1%.

2.3.2 Spacal

The main task of spacal is to provide precise measurement of the energy of the scattered electron, and to improve the quality of hadronic energy measurements in the backward region. It is divides into an electromagnetic section and a hadronic section, and consists of scintillating fibres embedded in a lead matrix, with readout by photomultiplier tubes. [11] The energy resolution of the electromagnetic section, determined from test beam measurements is approximately $7\%/\sqrt{E}$ with a constant term of 1%. For the hadronic section the resolution is about $13\%/\sqrt{E}$ for electrons and $70\%/\sqrt{E}$ for hadrons, with constant terms of 3.6% and 20% respectively.

2.3.3 The Plug Calorimeter

The plug calorimeter closes the gap in the acceptance for energy flow in the forward direction at small angles, between the beam pipe ($\theta \simeq 0.6°$) and the forward part of the LAC ($\theta \simeq 3°$). It consists of layers of copper absorber plates interleaved with layers of silicon detectors, and has a resolution of approximately $150\%/\sqrt{E}$.

2.4 Muon Detection

Muon identification is important, particularly for heavy flavour physics, but equally in the search for new or exotic particles. The identification and measurement of muons in the H1 detector is made up by two systems of detectors. Firstly, the instrumented iron detects muons emitted over the full solid angle, and in addition to this, the forward muon detector provides a means of independent momentum measurement of muons in the forward direction.

2.4.1 The Instrumented Iron

The iron yoke of the main solenoid which surrounds all the major detector components of H1 is instrumented with limited streamer tubes (LST) and readout pads, placed in slits between alternate layers of iron. These serve a dual purpose as a tail-catcher calorimeter to contain hadronic showers, and providing muon detection. Starting from the interaction point working outwards, there is firstly a muon box in front of the iron. This consists of two strip layers, and a third with pads. The first three slits in the iron are installed with pad layers, and the fourth houses two chambers (one strip and one pad layer). The remaining five slits are installed with pad layers, and behind the iron, there is another muon box. The limited streamer tubes provide a polar angular coverage of $5^\circ < \theta < 175^\circ$.

2.4.2 The Forward Muon Detector

The forward muon detector (FMD) [12] is designed to identify and measure the momentum of muons which have penetrated the instrumented iron in the polar angular range $3^\circ < \theta < 17^\circ$. It consists of six double layers of drift chambers, situated either side of a toroidal magnet. The magnet consists of eight solid iron modules built into two mobile half-toroids to allow access. The field inside varies with radius, from 1.75 Tesla at the inner radius (0.65m) to 1.5 Tesla at the outer radius (2.90m). The theta-phi-theta combination of layers (see figure 2.4) each side of the magnet allow the track of the muon to be fully reconstructed, whilst the bending of the track in the magnetic field gives a momentum measurement. The octants increase in size covering out to 4m diameter for the first plane (θ_1), to about 6m in diameter for the last (θ_4). The momentum resolution is limited by multiple scattering in the toroid, and increases slowly from about 25% for 5GeV muons to about 36% for muons at 200GeV. The four theta layers have wires strung around the beam pipe to provide an accurate measurement of the polar angle θ, and the two phi layers have wires strung radially, measuring the azimuthal angle, ϕ. Each layer is radially segmented into octants, which are mounted on either side of an aluminium door frame, with each door frame holding two octants and forming a quadrant. The door frames may be retracted to allow for access. The octants are built up of two planes of 12cm drift cells, offset from each other by half a cell's width, allowing for resolution of drift sign ambiguities as well as T-zero determination. The phi and theta octants are shown in

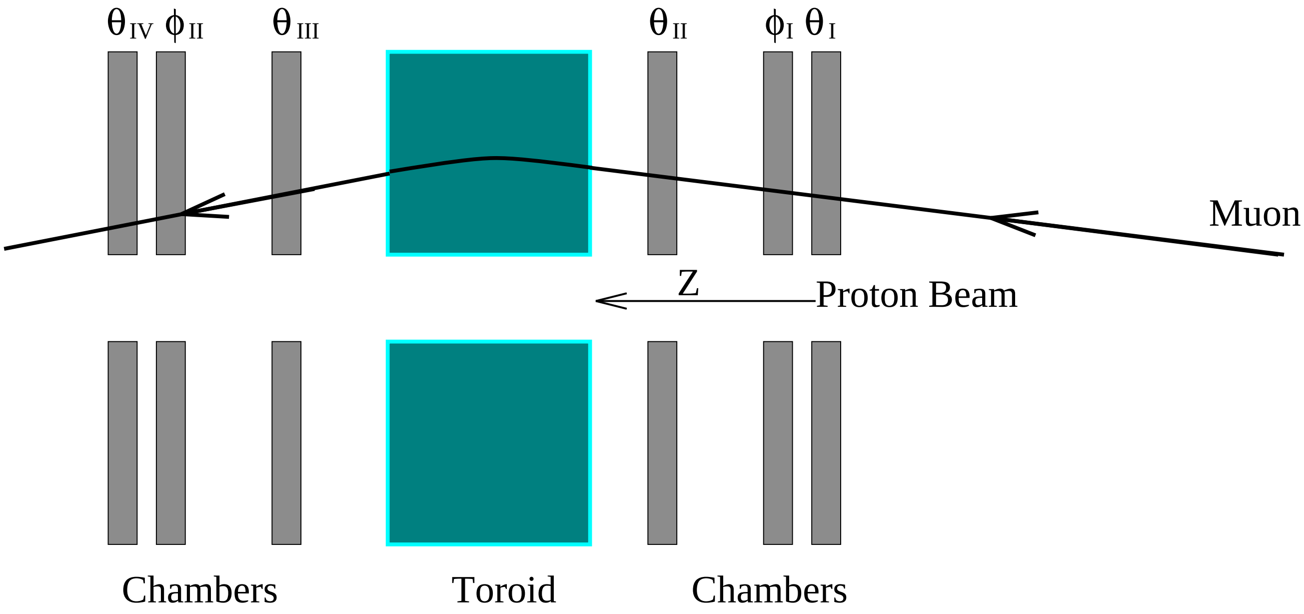

Figure 2.4: *Cross section view of the forward muon system.*

figures 2.5 and 2.6.

Each cell contains a single sense wire, one end of which is connected to a preamplifier, whilst the other is linked to the sense wire of the adjacent cell by a 330Ω resistor. The cells have 50μm thick Nichrome wires, except the short cells where the diameter is 40μm. For the long cells, there is a wire support in the middle. The gas mixture used in the drift chambers is 92.5% argon, 5% CO_2 and 2.5% methane.

Charge division gives a measurement along the wire, accurate to approximately 1% of the length of the sense wire, whilst the observed drift distance resolution is between 300 and 400μm.

Figure 2.6: *Theta Octant.*

2.5 The Luminosity System

The luminosity monitor consists of two components: an electron tagger and a photon tagger at 33m and 103m downstream of the interaction point respectively. The main objective is to detect the $e-\gamma$ coincidence from the the Bethe-Heitler process $ep \longrightarrow e\gamma\mathrm{p}$, which has a large and calculable cross section, allowing a measurement of luminosity to within 7% [4]. Both detectors are total absorption Cerenkov calorimeters with a resolution of $10\%/\sqrt{E}$. The electron tagger is also important in tagging photoproduction events.

2.6 Triggering

A sophisticated triggering system is necessary at H1 to distinguish between genuine electron-proton events and the high rate of background processes. Typical background events that need to be considered include photons or electrons from synchrotron radiation, interactions between proton or electron beams and the residual gas in the beam pipe or the wall of the beam pipe, and cosmic ray events. Background events outnumber interesting physics events by several orders of magnitude.

H1 is equipped with a multilevel trigger sytem, consisting of two hardware levels and two software levels. Only levels 1 and 4 have been implemented so far, with levels 2 and 3 being implemented this year. A first decision on an event is made after approximately 2.5μs at level 1, from the trigger elements from various subdetectors. A decision from level 1 to keep an event starts the readout, which can then be aborted at level 2 or level 3. Level 2, a hardware level, produces a decision within 20μs, whilst level 3, software level, makes a more complex study and produces a decision after a few hundred μs. The detector is effectively 'disabled' whilst the readout is being made, but this 'dead time' is minimized by the multilevel trigger system. If an event is accepted at level 3, the detector output is sent to the central data acquisition system so that a level 4 decision can be made.

Chapter 3

Alignment of the Forward Muon Detector

3.1 Introduction

Although the drift cells and sense wires are aligned precisely parallel and are positioned on an octant to within an accuracy of approximately 50μm perpendicular to the wire direction, the movement of the octants on the door frames (as required to allow access to the detector) has resulted in the octants within a layer becoming misaligned by the order of a cm or more. Translational misalignments occur along the beam direction and laterally with respect to the nominal positions, and there may also be rotational misalignments, *ie.* tilting of the octants with respect to the vertical plane. Recent work fastening the door frames together so that the whole system forms a rigid structure should eliminate this problem in future. Determination of the exact misalignment of each octant relative to others, to within the resolution of the detector, is necessary to exploit the potential precision for momentum measurements. Also it allows tighter chi squared cuts to be made on track finding in the reconstruction, hence cutting down on background.

Alignment of the forward muon detector can be carried out in two ways:-

- A physical survey.
- Using tracks passing through the detector.

In practice, a mixture of both these methods is used. Physical surveys are difficult due to the crowded environment around the forward muon system, however useful measurements of the relative z-positions of the theta layers have been made.

In order to determine translational misalignments in x and y it has been necessary to study tracks passing through the detector. The requirements for this study are a large number of straight tracks passing through corresponding octants in each layer, covering the full area of each octant. Cosmic muons are therefore best suited for the purposes of alignment. Since it is straight tracks that are needed, the toroid is switched off, and degaussed.

The following sections deal with the techniques used to calculate alignment values, results obtained, and various checks carried out to ensure the validity of the values subsequently entered in the database.

3.2 Physical Surveys

Physical surveys were carried out in March and November of 1994 [13], before the beginning and after the end of the 1994 running period respectively. The purpose of these surveys was to measure the relative z-displacements of the octants. In March, measurements were made between theta layers 1 and 2, and between theta layers 3 and 4. The measurements at the end of the running period (before the chambers were moved in any way) were between theta layers 2 and 3. No measurements were made of the positions of the phi chambers, because of the difficulty in getting to a suitable measuring point. Measurements were made between three points on corresponding octants in the layers concerned, so defining the plane of each octant, using a two metre rule, which was accurate to about 1mm.

3.3 Translational Alignment

Misalignments in z were taken into account using values from the physical surveys made of the detector, whilst misalignments in x and y were determined by a checksum method [14],[15], using a sample of cosmic muons taken in July. This latter method however, only gives relative values of misalignments, so in order to calculate absolute positions it has been necessary to assume that theta layers 2 and 3 have perfect alignment in x and y. To a certain extent, this decision is arbitrary, although it is thought that these layers are more likely to be well aligned with respect to H1. As long as the forward muon detector is aligned with respect to some internal coordinate system, the momentum measurement should not be affected, and any errors in alignment with respect to H1 should be small enough so that linking of forward muon tracks to tracks in other parts of the detector is not affected. In this analysis any rotational misalignments have not been taken into account.

The principle behind this method simply lies in comparing the gradients of different segments of a straight track. The gradient measured from $\theta_1 \rightarrow \theta_2$ should be the same as $\theta_2 \rightarrow \theta_3$, and similarly for $\theta_3 \rightarrow \theta_4$. Taking, for example, theta layer 1, this is expressed in the simple relation:

$$\frac{Y_2 - Y_1 - \Delta Y_1}{Z_2 - Z_1} = \frac{Y_3 - Y_2}{Z_3 - Z_2} \tag{3.1}$$

where ΔY_1 is the misalignment in y of one particular octant of theta layer 1. It can therefore been seen that a plot of the checksum:

$$(Y_2 - Y_1) - (Y_3 - Y_2)\frac{(Z_2 - Z_1)}{(Z_3 - Z_2)}$$

should have a mean centred on the misalignment in y for theta layer 1, ΔY_1. Large smearing effects occur due to the resolution and multiple scattering effects, and so high statistics are needed to give a good accuracy on the mean, ΔY_1. In order to achieve this, a sample of approximately 40000 cosmic muons was used. The effect of the multiple scattering of the muons in the toroid is to give the distribution a Breit-Wigner shape, with long tails. The values of z in the checksums are taken as the measured values. The various checksums used to determine the misalignment values in both x and y for theta layers 1 and 4 are listed in table 3.1. This process is repeated for each octant individually.

Misalignment quantities	Checksums used
ΔY_1	$(Y_2 - Y_1) - (Y_3 - Y_2) \times (Z_2 - Z_1)/(Z_3 - Z_2)$
$-\Delta Y_4$	$(Y_4 - Y_3) - (Y_3 - Y_2) \times (Z_4 - Z_3)/(Z_3 - Z_2)$
ΔX_1	$(X_2 - X_1) - (X_3 - X_2) \times (Z_2 - Z_1)/(Z_3 - Z_2)$
$-\Delta X_4$	$(X_4 - X_1) - (X_3 - X_2) \times (Z_4 - Z_3)/(Z_3 - Z_2)$

Table 3.1: *Table showing checksums used to determine misalignment values.*

3.4 Results

Examples of the checksums used to determine the various misalignment quantities are shown in figure 3.1, and these values are listed in table 3.2. in the local coordinate system of the forward muon detector.

3.5 Checks on alignment values

3.5.1 Using simulated data

A check on the checksum method for calculating misalignment quantities was carried out using simulated cosmic muons. The sample consisted of approximately 25000 muons with momenta ranging between 5 and 50 GeV and an angular range of $0° < \theta < 30°$ and $-180° < \phi < 180°$. Since these were for the purpose of alignment, the toroid was off. The simulation assumed perfect alignment, so in order to check the method used, the muons were reconstructed using some random misalignments (in theta layers 1 and

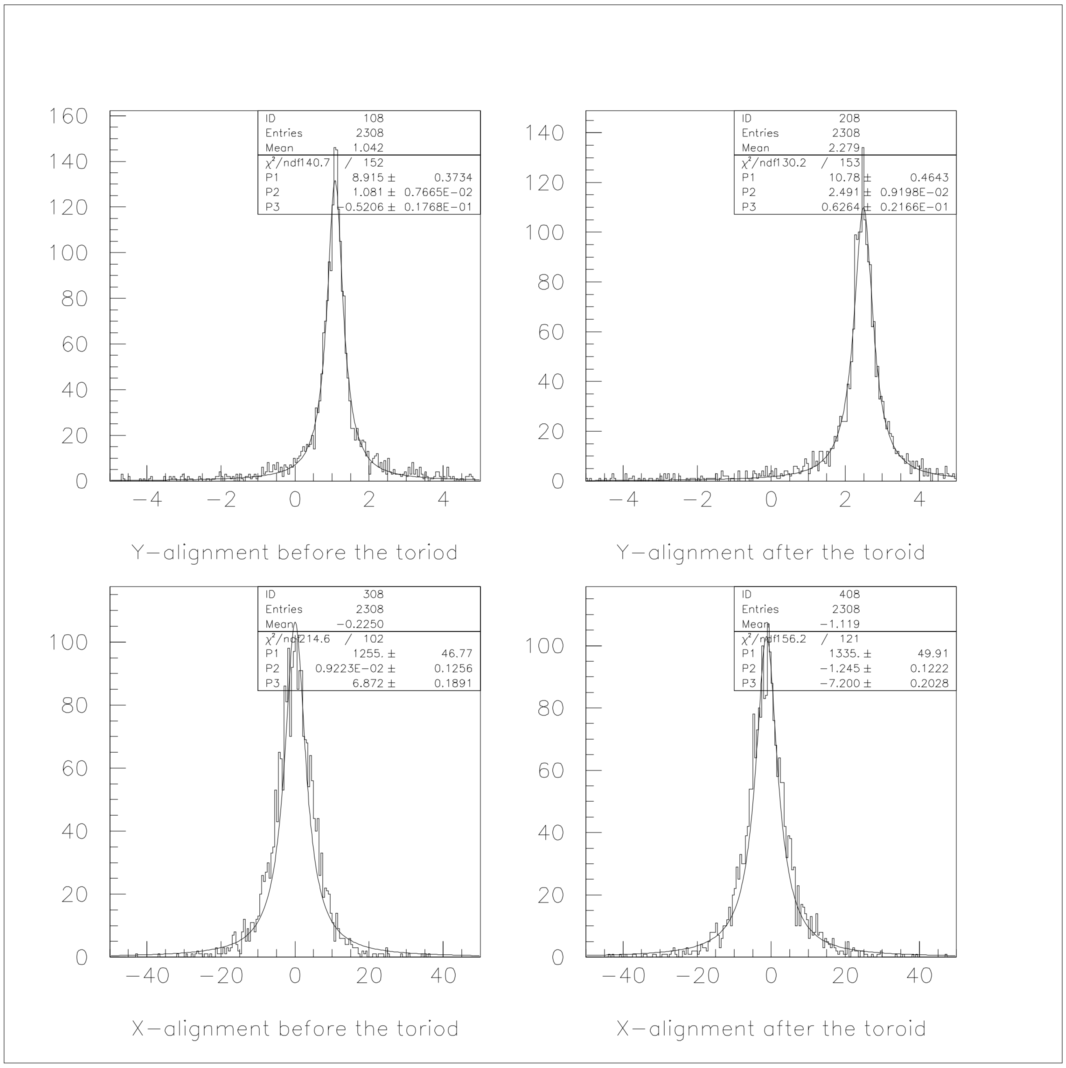

Figure 3.1: *Examples of checksums (for octant 8) used to determine alignment values.*

Octant	ΔY_1	$\sigma(\Delta Y_1)$	ΔX_1	$\sigma(\Delta X_1)$	ΔY_4	$\sigma(\Delta Y_4)$	ΔX_4	$\sigma(\Delta X_4)$
1	+0.937	0.011	+0.998	0.151	-2.515	0.010	-1.601	0.170
2	+0.388	0.008	+1.985	0.102	-1.838	0.007	-3.543	0.120
3	+0.458	0.009	-1.094	0.102	-0.620	0.007	-1.364	0.145
4	+0.419	0.008	+0.223	0.114	+0.599	0.008	-0.653	0.154
5	-0.002	0.009	+0.250	0.167	+1.468	0.008	-0.310	0.183
6	-0.130	0.008	-0.535	0.116	+1.007	0.008	+0.931	0.183
7	+0.650	0.011	-0.965	0.117	-0.941	0.006	+1.933	0.131
8	+1.081	0.008	+0.009	0.126	-2.490	0.009	+1.244	0.122

Table 3.2: *Misalignment quantities in cm*

4) in place of the usual alignment bank. The values then obtained from the checksums were compared to the given random misalignment values. This was done for x and y translational misalignments in theta layers 1 and 4. The results from these tests are shown in figure 3.2.

The calculated values have approximately the same values as the random misalignments given in place of the alignment bank, but have the sign reversed. This is to be expected since the misalignments were put in place using the alignment bank, and if the calculated values were then put back into this bank, the result would be no misalignment. It is also clearly seen that alignment in x is not as effective as alignment in y. This is because the x-coordinate, in the local coordinate system of the forward muon detector, refers to the charge division coordinate which is only accurate to approximately 3cm, whilst y refers to the drift coordinate, and is accurate to about 350μm.

3.5.2 Effects on reconstruction

A basic check on the alignment values calculated by the method described above is to run the reconstruction using the new values and see what effect

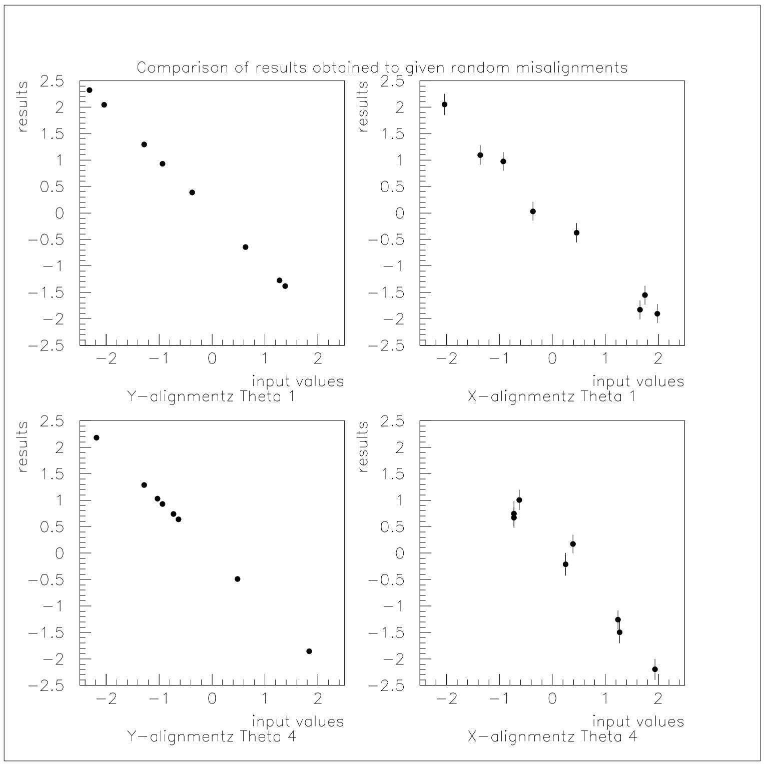

Figure 3.2: *A check on alignment procedure using simulated data: the plots show a comparison of the misalignments extracted by the the alignment procedure and the given misalignment values.*

it has on the tracks and segments subsequently found. This can also be used as a check to ensure the signs on the alignment numbers are correct. This was carried out using field on beam halo data, as this sample contains a high number of clean tracks. Figure 3.3 clearly shows that the use of the alignment bank increases dramatically the number of type 1 tracks found by the reconstruction. Type 1 and type 2 refer to the way the chi squares of the tracks are calculated. The chi squared is calculated after one segment has been extrapolated to the other to form a track, using the differences between the the x and y positions and the θ and ϕ. If this then passes the track

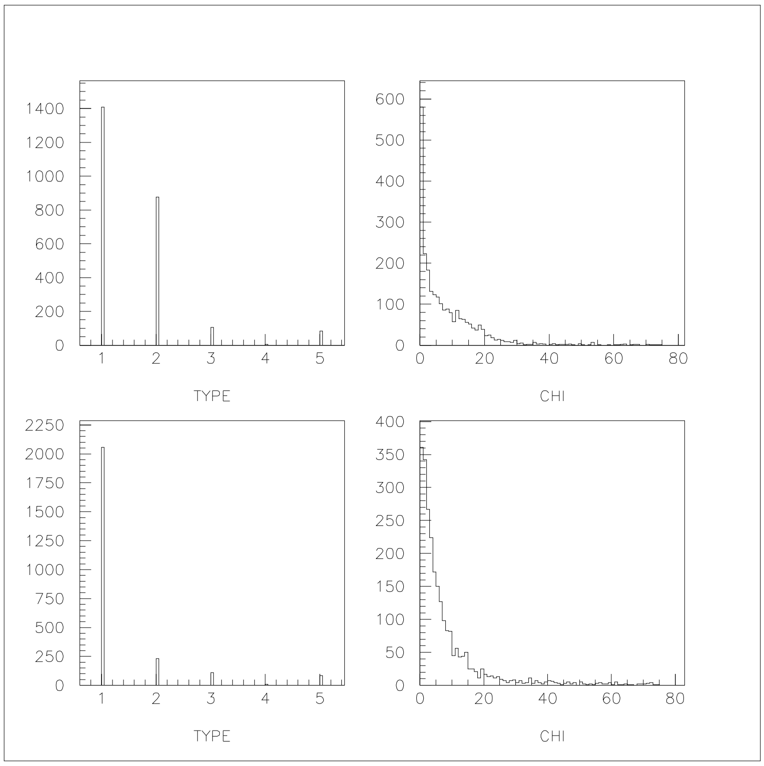

Figure 3.3: *The upper two plots show track types and track chi squareds for beam halo data reconstructed with no x or y alignment, and the lower two are the same plots with the alignment bank included in the reconstruction.*

finding chi squared cut, the track is classed as type 1. Tracks are classed as type 2 when the matching in x and y is not as good, and so the chi squared is calculated using differences in theta and phi only.

3.6 Rotational Alignment

Although it has been shown that including the translational misalignment values does improve the reconstruction to some extent, it also appears that including rotational misalignments should bring about further improvements.

Work is currently underway examining this possibility. By assuming that theta layers 2 and 3 do not suffer any rotational misalignment, the relative z measurements between theta layers 1 and 2, and between layers 3 and 4, can be used to define the planes of the octants in layers 1 and 4. In this way, the translational misalignments may be determined as described in section 4.3, but in the rotated frames of the individual octants, rather than the local coordinate frame of the forward muon system.

Once these misalignments are converted back to the local coordinate system of the FMD, the effects of the alignment on the reconstruction can be examined as discussed above. The results from these checks are shown in figure 3.4. These results look similar to those obtained simply using translational alignment, but work on rotational alignment is still in progress. Further work checking the process of rotational alignment using simulated data is also needed. Another simple check on the values obtained is to put them back through the alignment process, and recalculated the misalignments. The results from this check are shown in figure 3.5, and, as expected, the checksums yield misalignment values which are zero within errors.

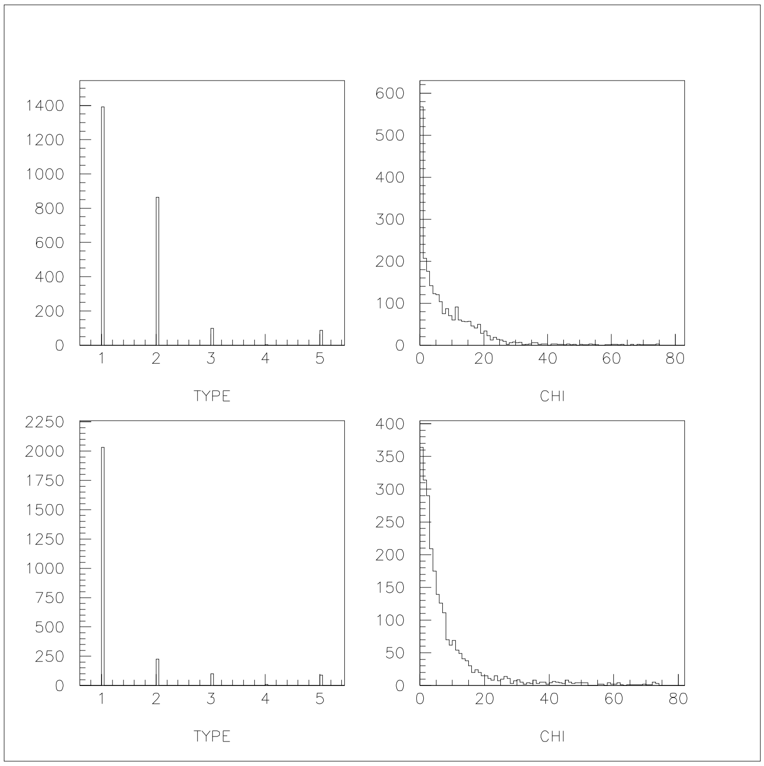

Figure 3.4: *Plots showing the affect of rotational alignment on reconstructing beam halo data. The upper two plots show track types and track chi squareds for reconstructed data with no alignment, and the upper two plots show the same quantities for data reconstructed with rotational alignment.*

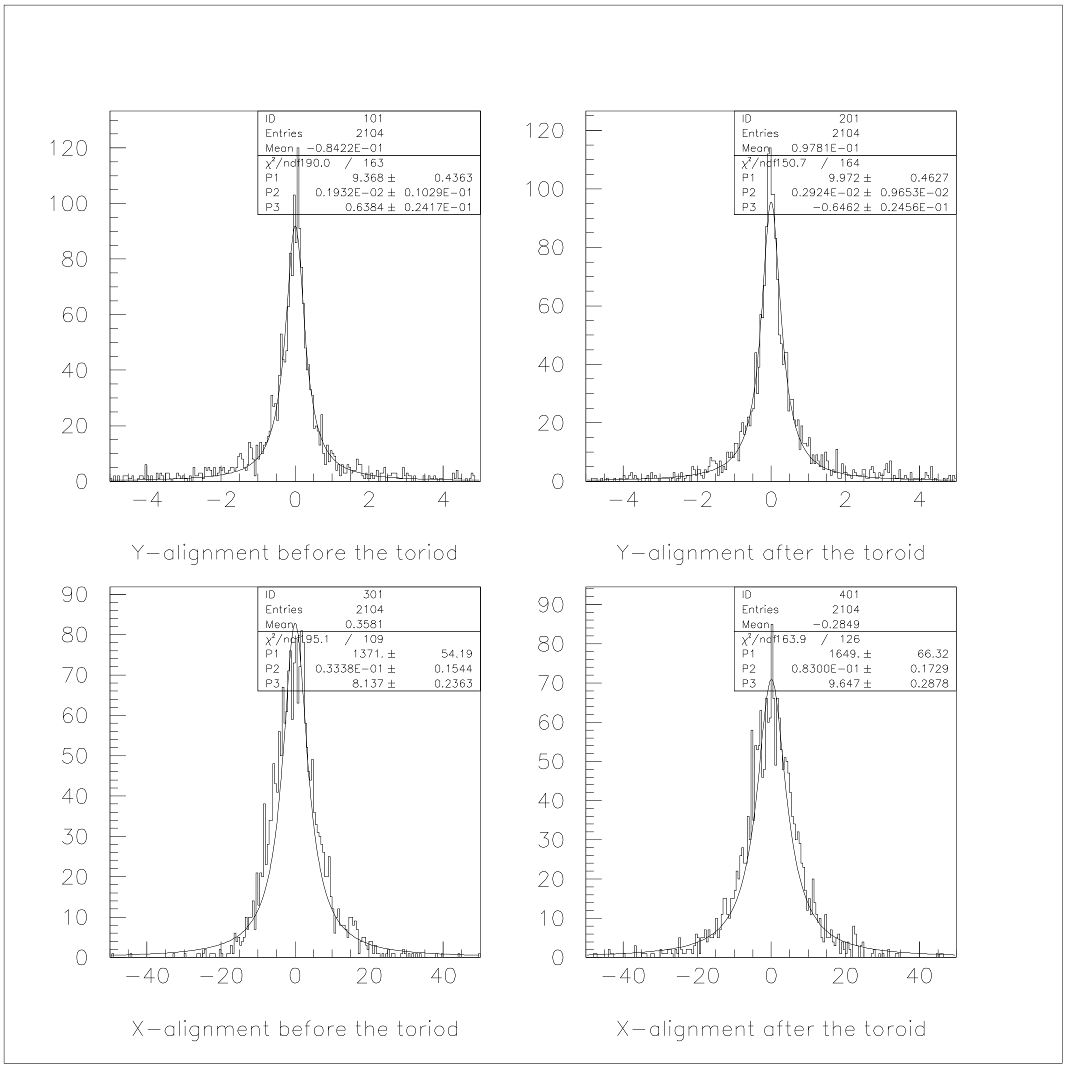

Figure 3.5: *Examples of checksums obtained (octant 1 only) when both translational and rotational alignment quantities are included.*

Chapter 4

Drift Velocity and T-zero Studies

4.1 Introduction

When a muon passes through a drift cell, the electrons produced from the resulting ionization drift towards the sense wire, and once they get very close to the wire, the strong electric field produces an ‘avalanche effect’. This produces a pulse which propagates in both directions along the wire, and is collected by the readout. Online analysis of the pulses gives information on the time taken for the electrons to drift from the path of the muon to the sense wire, and on the integrated charge at the two wire ends. This is known as the Qt information. In order to reconstruct a muon track it is necessary to convert the raw times and charge information to space points. The distance along a sense wire (the x coordinate in the local coordinate system of the forward muon system) is determined from charge division, by comparing pulse heights from both ends of the wire. The drift distance (the y coordinate) is found using the raw drift time, the drift velocity, v, and the T-zero.

The drift velocity, *ie.* the the speed at which primary electrons move through the gas in the drift cell, depends on the electric field in that cell, and on the gas pressure. If the velocity is too high, the distance resolution is reduced, since it is dependent on the constant time resolution of the FADC's. If it is too low, then the pulses may arrive outside the FADC time bin window and not be read out, or not give enough time for the trigger to make a decision on the event at level 1. Studies carried out at Manchester on the variation of the drift velocity with pressure and drift field, show that the drift velocity reaches a 'plateau' (see figure 4.1) [16] at the maximum of the curve where slight variations in field or pressure should not greatly affect it.

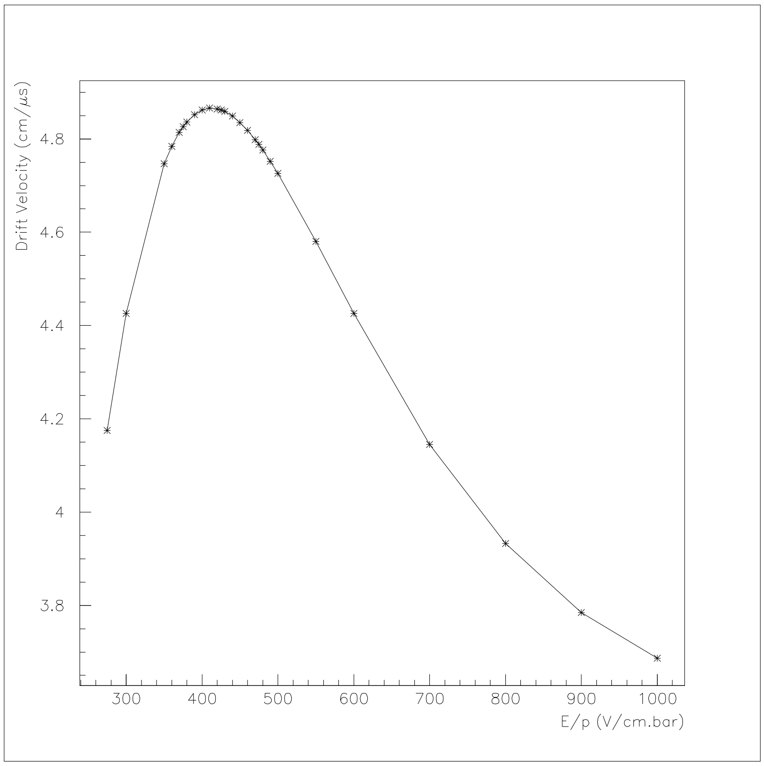

Figure 4.1: *Variation of drift velocity with E/p.*

The determination of the drift time involves taking into account the time of flight, as well as the relative time differences between the cells (due to differences in wire length *etc.*) which is done using test pulse runs. This gives a corrected time, T_{cor}, and the drift time is then given by:-

$$T_{drift} = T_{cor} - T_0 \tag{4.1}$$

where T_0 is a constant, the global T-zero. T_0 can be explicitly defined as the corrected time obtained for a muon passing very close to the sense wire.

Determination of both v and T_0 requires a large sample of muons in time with the HERA clock, triggered by the H1 central trigger, free from background, and at low angles. Physics muons were considered unsuitable because of the large background and small rate, and cosmic muons could not be used as they are out of time with the HERA clock and leave steep tracks. The studies described in this chapter were carried out using beam halo data. All the beam halo data available for the 1994 running period was analysed.

The rest of this chapter will deal with how the drift velocity and T-zero are calculated, and the results obtained.

4.2 Determination of Drift Velocity

The drift velocity may be determined from the time distribution [14]. The smearing at the edges of the top hat distribution is due to a non-zero spatial resolution and also a variation in drift velocity in some regions of the cell. An ideal drift cell would have constant drift velocity across the whole volume, but in reality this is limited to certain regions of the drift space. The regions of a drift cell where the drift velocity is not constant occur as a result of a non-uniform electric field at the edges of the cell and very close to the sense wire. In determining the drift velocity, the region of the time distribution which is constant is chosen, as this corresponds to a region of constant drift velocity. If the number of events within this region is N_{mid}, and the length of the chosen region is D_{mid}, then

$$D_{mid} = \frac{N_{mid}.D}{N} \tag{4.2}$$

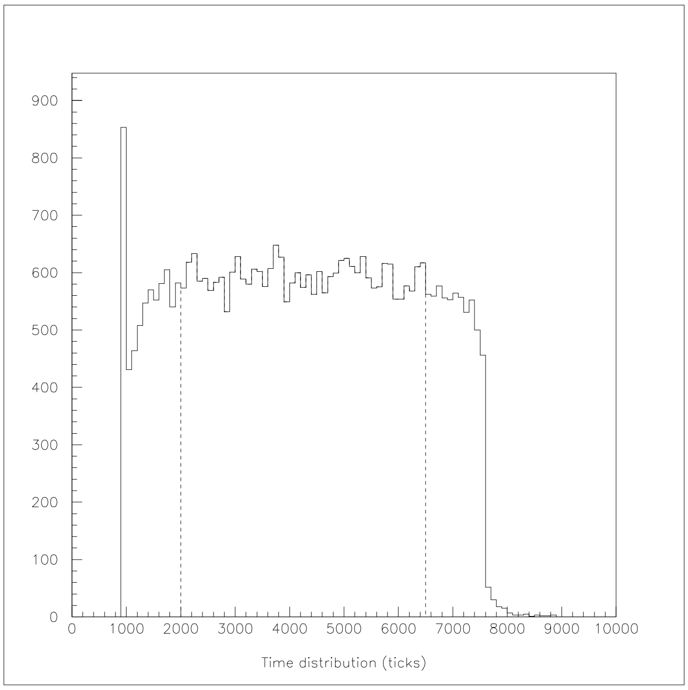

Figure 4.2: *Time distribution, and middle range of time distribution.*

where D is the total drift length and N is the total number of events. The time distribution is shown in figure 4.2, with the middle range marked with dotted lines. Since the drift velocity, v is constant and $v = D_{mid}/\Delta T$, then

$$v = \frac{N_{mid}.D}{N.\Delta T} \tag{4.3}$$

where ΔT is the length of the chosen region in time.

The large peak in the first time bin of the time distribution occurs as a result of a T_0 which is too large being used in the reconstruction. Since the T_0 must be subtracted to give the corrected time (equation 4.1), the value for this corrected time may be less than zero if the T_0 is too large. When this occurs, the events fall into the first time bin. This does not effect the determination of drift velocity, since it is simply the ratio of the number of events in each plot which is used in the calculation.

4.3 Determination of T-zero

The determination of T-zero is done in two stages. Firstly, the value of T_{mid} is calculated. T_{mid} is defined as the drift time for a distance of 3cm, namely half the maximum drift distance. T_{mid} can be calculated in one of two ways. It can be taken as the mid-point of the time distribution, or, more accurately, determined using a checksum [14]. The checksum in this case does not involve an entire track, but can be calculated from a segment either before or after the toroid independently. For a straight segment, the gradient as measured by the two sublayers of θ_1 should be the same as the gradient as measured by the two sublayers of θ_2. Depending on the 'stagger' permutation of the cells this method yields two possible checksums, as shown in figure 4.3. The first checksum, which defines the quantity T_{mid}, can also be written as:

$$T1 + T2 + T3 + T4 = \frac{12cm}{v} + 4T_0 \tag{4.4}$$

T_{mid} can therefore be determined by plotting the above checksum, and once the drift velocity is known, then the T-zero is given by the simple equation:

$$T_0 = T_{mid} - \frac{3cm}{v} \tag{4.5}$$

The first checksum, which defines the quantity T_{mid}, can also be written as:

$$T1 + T2 + T3 + T4 = \frac{12cm}{v} + 4T_0 \tag{4.6}$$

T_{mid} can therefore be determined by plotting the above checksum, and once the drift velocity is known, then the T-zero is given by the simple equation:

$$T_0 = T_{mid} - \frac{3cm}{v} \tag{4.7}$$

The drift distance resolution may be determined from the width of the other checksum (see figure 4.4).

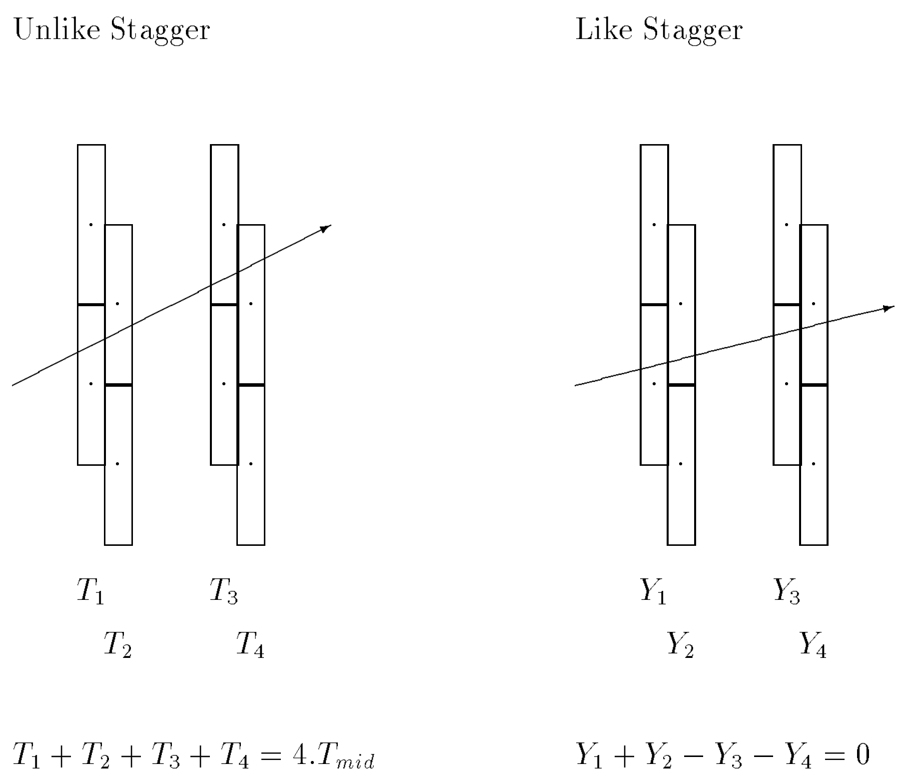

Figure 4.3: *The two possible stagger permutations of the cells, for a track through two layers.*

4.4 Variation of Drift Velocity and T-zero

It is important not just to know the precise values of the drift velocity and T-zero, but also whether or not they change over time. In order to investigate this, the values of these quantities were determined over the whole run period. This was done by calculating the drift velocity and T-zero from samples of beam halo data taken over a period of several runs, which was necessary to ensure that there were enough statistics. In this way, all the beam halo data for 1994 was analysed, except for the period of time when the forward muon

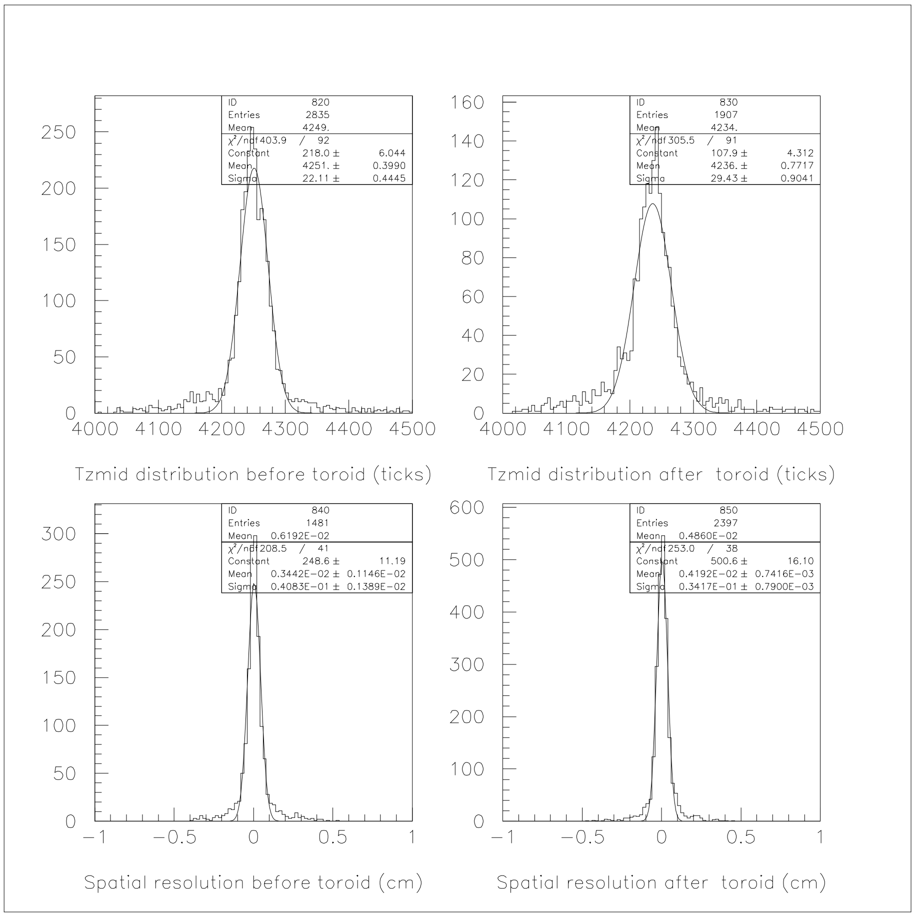

Figure 4.4: *Checksums for T_{mid} and y-resolutions before and after the toroid.*

detector was not fully operational.

4.5 Results

The variations of drift velocity, T_{mid} and T-zero over the 1994 running period are shown in figure 4.5. The gap in results between runs 87297 and 88367 is the period when the forward muon detector was not fully operational. Due to problems with synchrotron radiation, theta 4 was switched off for much of this time. Also, the points in the period between runs 82005 and 82962 are not reliable as this was the change over period from running with electrons to running with positrons. An interesting feature to note in the first plot is the steady fall in drift velocity over the electron running period, *ie.* up to run 82005. The reasons for this are not understood, although it may be related to a slow change in gas composition. The value of T-zero shows a clear jump around run 88400, which was expected as a result of changes made to the FADC and readout electronics. Also, there is a correlation between the measured drift velocity and the T-zero, whereas the T_{mid} stays relatively constant over the whole run period. Further studies to understand this effect are clearly necessary.

Previously the values of T-zero and drift velocity for the forward muon detector in the database had been assumed to be constant over the whole run period. In order to improve on this, the run period was divided into seven periods of approximately constant T_0 and v, and the values put into the database were averages of the values calculated for these quantities over the different periods of time (see figure 4.6).

The change in the resolution of the drift distance was also examined over the whole run period, and the results for this are shown in figure 4.7. The reasons for the change in the resolution over time are not understood, but it is clear that this effect needs investigating to ensure optimum resolution for the forward muon detector during next year's running.

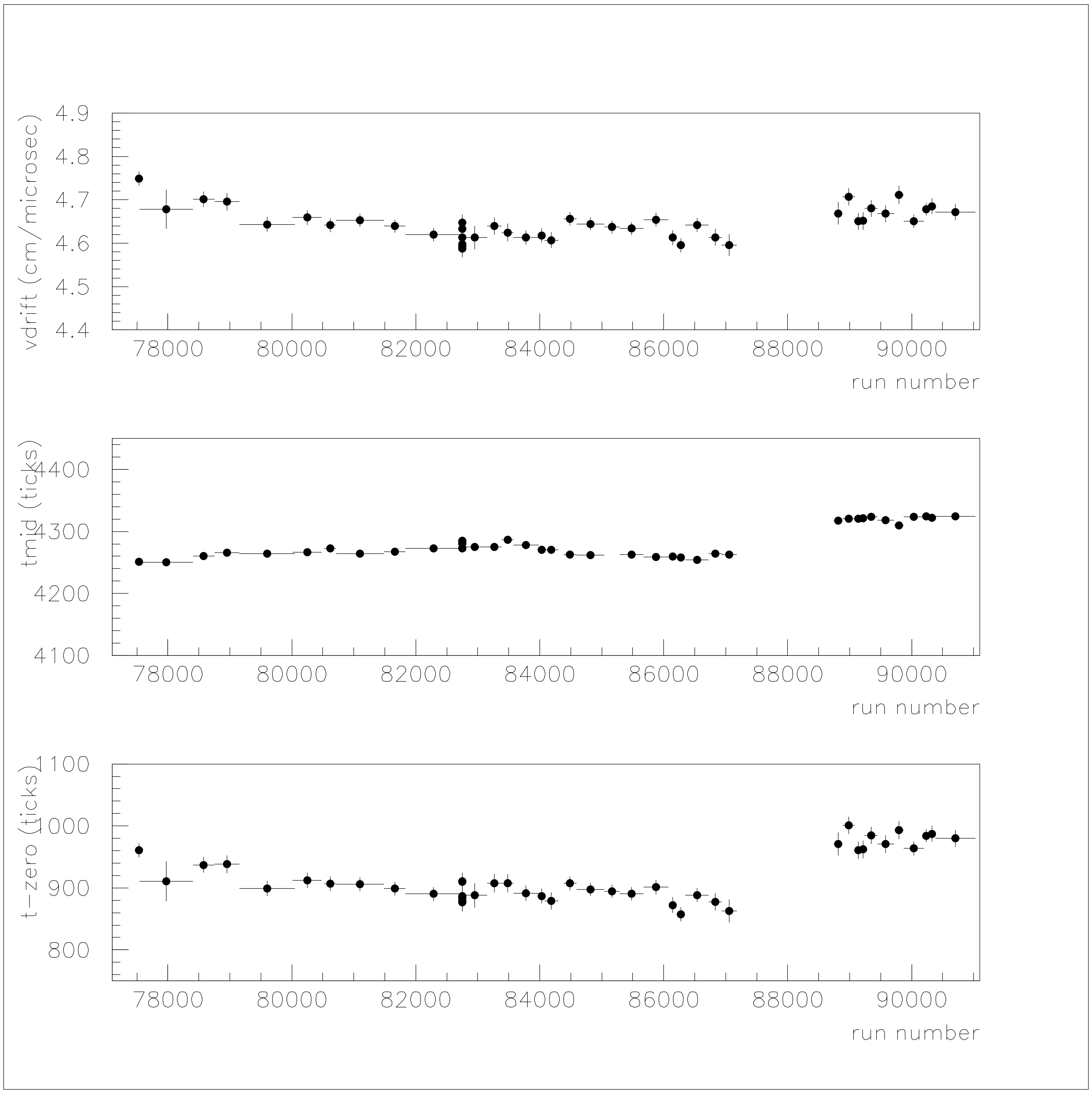

Figure 4.5: *Plots showing the variation of drift velocity,* T_{mid} *and T-zero over the 1994 run period. The vertical error bars show statistical errors, and the horizontal bars refer to the period of runs over which the quantity was determined.*

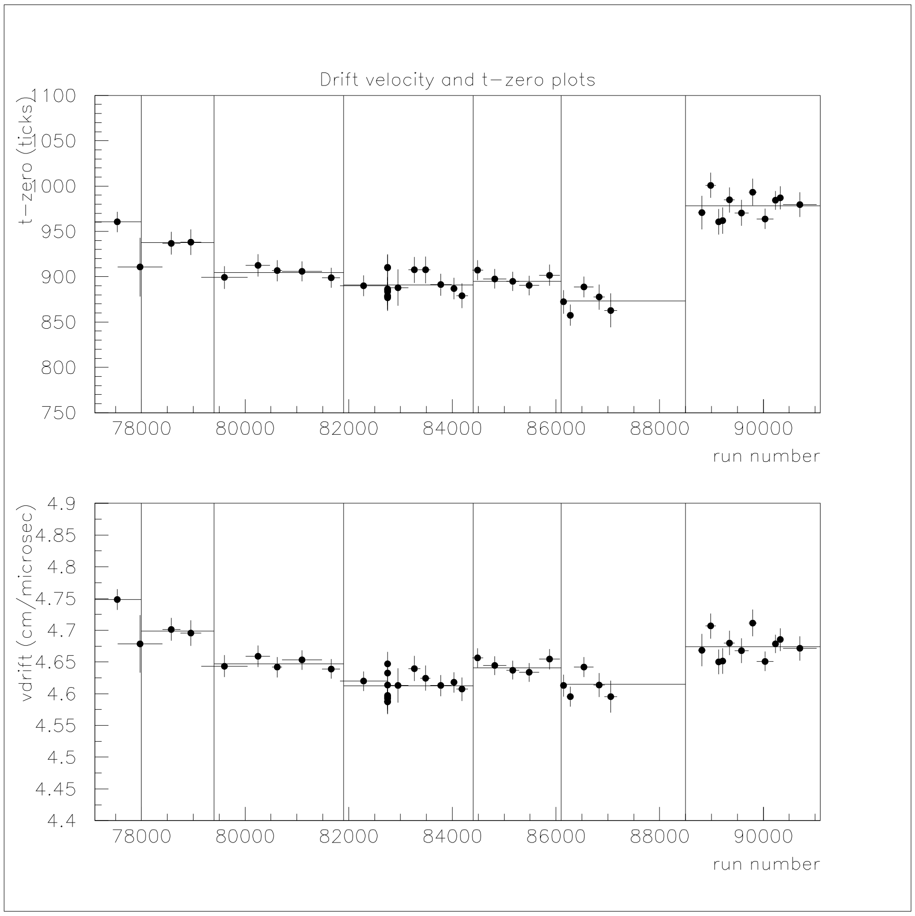

Figure 4.6: *Average values for T-zero and drift velocity in the database for the 1994 run period.*

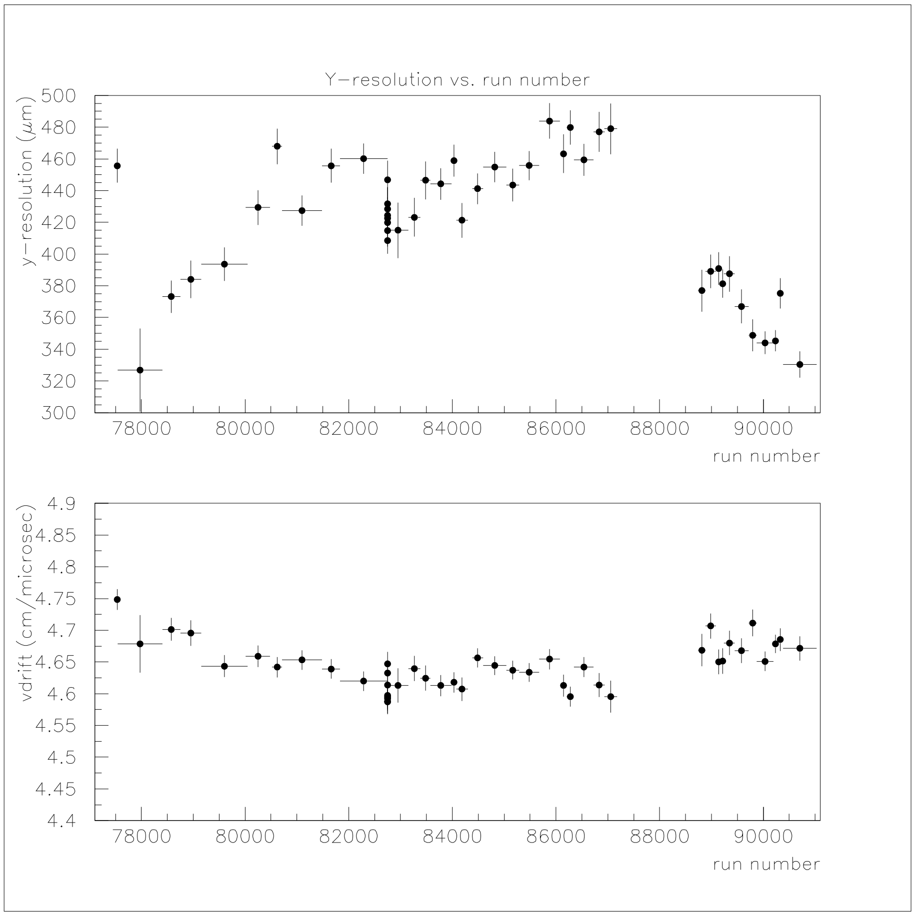

Figure 4.7: *Change in the drift distance resolution over the 1994 running period. For comparison, the variation in drift velocity is shown beneath.*

Chapter 5

A Search for J/ψ to Dimuon Events in the Forward Muon System

5.1 Preliminary Search

A preliminary search was carried out for elastic J/ψ events, where the J/ψ decayed to two muons, with at least one of these passing through the forward muon detector. For this type of event, the only visible tracks in the H1 detector should be the two muon tracks. (The mechanism for elastic J/ψ production was discussed in section 1.3.3.)

The data sample examined was all the data with a forward muon trigger from the period when HERA was running with electron - proton collisions, *ie.* up to run 82005, which corresponds to an integrated luminosity of approximately 500nb^{-1}. The forward muon trigger requires a track through the forward muon system with an associated track through the forward endcap of the instrumented iron. There are also the standard additional requirements of good vertex and t-zero determination, together with a background veto requirement.

The cuts applied to this sample were kept as loose as possible, simply demanding either at least two tracks in the forward muon detector, or one through the FMD and at least one other track elsewhere in the instrumented iron. A cut was also made on beam halo background by demanding no veto wall trigger. The events remaining were then scanned by eye. A total of 5 J/ψ candidates were observed, two of which had both muons passing through the FMD. Figure 5.1 shows an elastic J/ψ candidate, where both of the muons pass through the forward muon system. The invariant mass was approximately 3.2GeV.

5.2 Generated J/ψ Events

Generated events of elastic J/ψ production, where the J/ψ decays to two muons, were used to obtain an estimation of the number of J/ψ to dimuon events that should have been seen by the forward muon detector. Two sets of cuts were applied to this sample. Firstly, that the polar angle for both particles was in the range $4° < \theta < 17°$ and the momentum of both particles was greater than 5GeV. This corresponds to both muons passing through the forward muon system. The second set of cuts corresponded to one muon passing through the FMD and one elsewhere in the iron, *ie.* the above cuts for one muon, where the other muon has a polar angle $\theta > 17°$ and momentum $p > 1.5$ GeV. These cuts only approximately model the true acceptances for muon detection, and in order to get a better idea of these acceptances, a full simulation would be required. However, this is not neccessary for the purposes of this study, which simply gives an initial rough estimate of the reconstruction and trigger efficiencies, and is limited by low statistics.

From these assumptions, the estimated numbers were found to be 6.65% of dimuon events with both muons passing through the FMD, and 24.7% with one muon in the FMD, and one elsewhere in the detector. Using a cross section for elastic J/ψ production of 2.5nb and a branching ratio of

6%, for J/$\psi \longrightarrow \mu^+\mu^-$, an estimate for the numbers of these events that should be observed can be made. However, since these events are at the generator level, the efficiencies and acceptances of the various subtriggers and the reconstruction are not taken into account. It was estimated that approximately six events should occur where both the muons pass through the FMD, and approximately 18 events where one passed through the FMD and one elsewhere in the detector. Another consideration is that the numbers estimated do not take into account any background events. The cross section of 2.5nb is for J/ψ produced elastically via pomeron exchange, but photon - gluon fusion events may appear to be elastic if the proton remnant is not detected. Also, any QED background has not been taken into account, so a cross section of 2.5 is a conservative estimate; and in addition recent studies indicate that the true value is higher.

5.3 Conclusions and Future Work

There is a clear discrepancy between the number of expected events and the number observed, which gives a first indication of the efficiencies of the reconstruction and the forward muon trigger, but further work is necessary to ascertain where difficulties lie. In principle it is possible to separate the efficiencies for the trigger and track reconstruction from the above results; however present statistics do not allow this to be achieved with any degree of accuracy.

Preliminary studies of the forward muon trigger element efficiency indicate that it is of the order of 70% for events with a good z-vertex and muons with momentum of 4GeV or more in the forward muon system, but for muons with momentum lower than this, the efficiency begins to drop.

Future work would include studies of the efficiency of the full forward muon subtrigger. To achieve this a sample of forward muon data which did not require a forward muon trigger or reconstructed forward muon track would be used. For example, data which had a forward inner iron endcap subtrigger, but did not demand a forward muon trigger element would be suitable. Scanning this data by eye to ascertain how many events had forward muon track, and of these how many had been triggered and/or reconstructed, would give a good estimate of these efficiencies. Also, completion of work on rotational alignment is important before the 1995 running period, to maximize the track finding efficiency of the reconstruction. This work should ensure that interesting physics events are not missed, and the forward muon system can fulfill its potential in the study of heavy flavour physics.

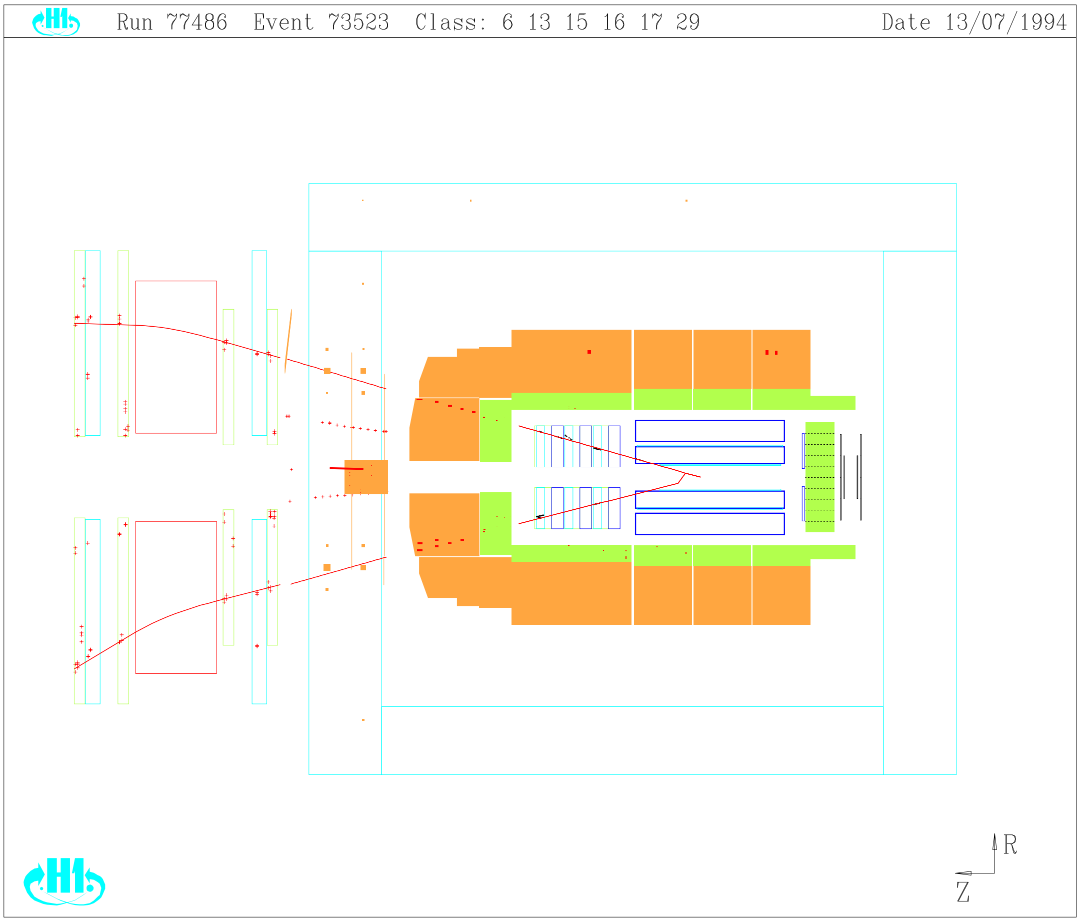

Figure 5.1: *Elastic J/ψ decaying to two muons.*

Bibliography

[1] 'Physics at HERA Workshop Proceedings' vol 1-3 DESY (1991)

[2] C.Kiesling, 'Physics from the First Year of H1 at HERA', DESY 94-137 (1994)

[3] H.U.Martyn, 'Recent Results from the H1 Experiment at HERA', DESY 94-195 (1994)

[4] B.Burow, 'Results from Zeus and H1 Experiments at HERA on the Total Photoproduction Cross Section and its Contributions', DESY 94-215 (1994)

[5] H.Jung et al., 'J/ψ Production Mechanisms and Determination of the Gluon Density at HERA (Proceedings of the HERA Workshop', vol 2) (1991)

[6] H1 Collaboration, 'Photoproduction of J/ψ Mesons at HERA

[7] H1 Collaboration. 'A Search for leptoquarks and squarks at HERA', Z Phys. C64, 545-558 (1994)

[8] H1 Collaboration, 'The H1 Detector at HERA', DESY 92-103 (1993)

[9] H1 Collaboration, 'Technical Proposal to Upgrade the Backward Scattering Region of the H1 Detector', (1993)

[10] H1 Collaboration, 'Technical Proposal to Build Silicon Tracking Detectors for H1', (1992)

[11] G.Mueller, 'A Spagetti Calorimeter for the H1 Detector', (for the proceedings of the 5th International Conference on Calorimetry in High Energy Physics.)

[12] I.Kenyon et al., 'The Forward Muon Spectrometer', DESY 93-020 (1993)

[13] P.Biddulph, Forward Muon Alignment Measurements notes, 1994.

[14] J.P.Sutton, 'The H1 Forward Muon Spectrometer at the HERA Collider', (Doctoral Thesis, Manchester University, 1993)

[15] A.Mehta, 'Calibration of the Forward Muon Detector and Determination of the Diffractive Proton Structure Function ar H1', (Doctoral Thesis, Manchester University, 1994)

[16] R.K.Griffiths, 'Drift Chamber Calibration using Laser ionization', (MSc. Thesis, Manchester University, 1994)